Optical dichroism of nickel in diamond

1992 J. Phys.: Condens. Matter 4 775

(http://iopscience.iop.org/0953-8984/4/3/017)

J. Phys.: Condens. Matter 4 (1992) 775–784. Printed in the UK

Optical dichroism of nickel in diamond

L Paslovsky and J E Lowther
Department of Physics, University of Witwatersrand, Johannesburg, South Africa

Received 3 July 1991

Abstract. Recent optical measurements of a 1.4 eV doublet in diamond have revealed distinct optical polarization features which are associated with a nickel defect. A model for the defect is investigated taking into account the large electronic hybridization that will take place about the metal ion. Relative spectroscopic intensities and estimates of the spin–orbit interaction are considered within the LCAO approximation. Finally, a cluster model calculation is made specifically to investigate the electronic structure of the nickel defect and estimate the LCAO coefficients. From the results, suggestions are made about the possible charge states and lattice locations of nickel in diamond.

1. Introduction

When nickel is incorporated into synthetic diamond distinct optical features around 1.4, 1.88, 2.51 and 3.1 eV are observed in absorption spectra, with the 1.4 eV feature and a 2.56 feature observed in cathodoluminescence (Collins *et al* 1983, Davies *et al* 1989, Collins *et al* 1990). The spectra are tentatively associated with nickel—although at present there is no firm indication that the 1.4 eV system and the 1.88/2.51/3.1 eV systems arise from the same form of defect. The 1.4 eV feature, which we shall be primarily concerned with here, consists of a zero phonon doublet which is separated by 2.7 meV, and it has been shown (Collins *et al* 1983, Davies *et al* 1989) that the transition is associated with a nickel defect with the doublet arising from a slight splitting of the ground state. A unique feature of the 1.4 eV transition is its strong polarization properties which are visible in both cathodoluminescence and optical absorption spectra (Collins 1989). The higher energy component of the doublet (at 1.4035 eV) is observed only under a π polarization whereas the lower energy component (at 1.4008 eV) is seen in both σ and π polarizations with Collins explicitly reporting that the σ to π polarizations in the low energy component differ by roughly 30%. More recently Nazare *et al* (1991) using high resolution piezospectroscopy have deduced the orbital character of the two states involved in the 1.4 eV transition. They find, in addition to the energy levels changing with application of stress, that each line is split with application of an external magnetic field. It was concluded that the states involved have ^{2}E and ^{2}A symmetry in the point group C_{3v}.

The electronic origin of the doublet though is not clear. Collins (1989) suggest that the doublet arises because of some kind of dimer pairing mechanism across nickel atoms which are stacked along the ⟨111⟩ crystallographic planes. Alternatively Nazare *et al* (1991) speculate that the splitting is due to a spin–orbit interaction. In this paper we shall explore the latter idea.

0953-8984/92/030775 + 10 $03.50

2. Electron states of transition metal ions in covalent solids

Although much experimental knowledge is available about transition metal ions in covalent solids, the origin of the levels is complicated because of the possibility of a strong covalent hybridization with the host lattice and associated change in ionic configuration of the metal. In early work concerning transition metal ions in silicon Ludwig and Woodbury (1962) put forward the suggestion that the metal ion would hybridize with the host lattice to the extent that on a substitutional site an ionic configuration of the form $3d^{\alpha}4s4p^3$ would result, the $4s4p^3$ configuration then being typical of the directed covalent bonding in the host. In the case of the interstitial transition metal ion impurity it was suggested that hybridization would stabilize the ion at the site through a strengthening of the back bonds on adjacent atoms. On the basis of such models Ludwig and Woodbury were able to analyse details of the ESR spectra due to several transition metal ions in silicon.

Along with the experimental effort, there has also been much theoretical work and this has been reviewed recently by Zunger (1986). As Zunger points out, the details of the electronic structure of transition metal ions in solids are complicated not only because of the strong electron correlation at the ion but also because transition metal ions could induce quite a considerable relaxation of the lattice. Such a relaxation could extend over quite some distance in the lattice and therefore is extremely difficult to calculate. Despite these complexities, some time earlier Haldane and Anderson (1976) in their theoretical study of transition metals in silicon deduced that several gap levels could be associated with a metal ion, these levels being closely spaced in energy and associated with the different charge states of the ion. From a molecular orbital viewpoint, the Haldane and Anderson concept reflects the importance of one-electron gap states and the associated large hybridization effects. Thus, when considering the electronic states of transition metals in semiconductors and, in particular, diamond we must describe the electron states to incorporate large hybridization—especially including metal 4s and 4p ionic configurations.

2.1. LCAO description at C_{3v} sites

We shall use the one-electron description initially to describe the state of the defect in diamond. From Group Theory (Griffiths 1964, Bates 1968) the transition metal ion states give rise to one-electron levels with $t_2(\xi, \eta, \zeta)$ and $e(\theta, \varepsilon)$ symmetries, both of which contain varying contributions of metal 3d, 4s or 4p as well as ligand carbon states. In the case of a C_{3v} symmetry, the t and e state will split into $a_1(z)$ and $e(x, y)$ states respectively as discussed in the Appendix. Relating the C_{3v} states to those of the group T_d from symmetry (see Griffiths 1964) we have, for their description in terms of atomic orbitals,

$$\left.\begin{aligned} x &= a_e d_\theta - a_t((d_\xi + d_\eta - 2d_\zeta)/\sqrt{6}) + a_p((p_x - p_y)/\sqrt{2}) \\ y &= a_e d_\varepsilon + a_t((d_\xi - d_\eta)/\sqrt{2}) + a_p((p_x + p_y - 2p_z)/\sqrt{6}) \end{aligned}\right\} \quad C_{3v}(e) \qquad (1)$$

$$z = b_t((d_\xi + d_\eta + d_\zeta)/\sqrt{3}) + b_p((p_x + p_y + p_z)/\sqrt{3}) + b_s(s) \qquad C_{3v}(a_1) \qquad (2a)$$

$$\left.\begin{aligned} x &= c_e d_\theta - c_t((d_\xi + d_\eta - 2d_\zeta)/\sqrt{6}) + c_p((p_x - p_y)/\sqrt{2}) \\ y &= c_e d_\varepsilon + c_t((d_\xi - d_\eta)/\sqrt{2}) + c_p((p_x + p_y - 2p_z)\sqrt{6}) \end{aligned}\right\} \quad C_{3v}(e) \qquad (2b)$$

where the LCAO coefficients will have to be obtained from some numerical calculation.

Table 1. Relative transition probabilities from the t_2 derived spin–orbit states of C_{3v} to the two e derived spin orbit states of C_{3v} as indicated in figure 2(*c*). E_x is measured along the cubic $\langle 1-10\rangle$ direction, E_y along $\langle 11-2\rangle$ and E_z along $\langle 111\rangle$.

	E_z	E_x	E_y
ψ_1:	$2\beta^2P$	α^2S	α^2S
ψ_2:	0	$2\beta^2Q + \alpha^2S$	$2\beta^2Q + \alpha^2S$

2.2. *Inclusion of spin–orbit coupling*

An additional perturbation to the system brought about by spin–orbit coupling causes splitting of these states. To evaluate the magnitude of this in the $(\Gamma_4 + \Gamma_5)$ and Γ_6 system we consider inclusion of spin–orbit coupling by means of the usual Hamiltonian $\mathcal{H} = \lambda \boldsymbol{L} \cdot \boldsymbol{S}$. Expressed in terms of the LCAO coefficients of (1) we find that the spin–orbit splitting in the upper e state, as shown in figure A2 of the appendix, is

$$\Omega = 2\lambda(\sqrt{2}a_e a_t + a_t^2/2). \tag{3}$$

Here we assume that the spin–orbit coupling interaction is primarily on the metal atom and we use the value $\lambda = 40$ meV for atomic nickel (Dunn 1961). This can be justified first that the spin–orbit interaction is of a short range (αr^{-3}) and second, especially in the case of diamond, that spin–orbit coupling about carbon is very small.

2.3. *Optical transition probabilities*

The relative optical dipole polarization matrix elements can also be obtained in terms of the LCAO coefficients given in (1) and (2). Particularly for transitions to the e derived spin–orbit states indicated in figure A2, these polarization elements are given in table 1 where the parameters employed are expressed in terms of the LCAO coefficients of (1) and (2) and are

$$\begin{aligned} P &= [\sqrt{2}(a_e c_p - a_p c_e)R_1 - (a_t c_p - a_p c_t)R_1]^2 \\ Q &= [(a_e c_p + a_p c_e)R_1 + \sqrt{2}(a_t c_p + a_p c_t)R_1]^2 \\ S &= [(\sqrt{2}a_e b_p - a_p b_e)R_1]^2 + [(a_p b_s)R_2 - (a_p b_t)R_1]^2. \end{aligned} \tag{4}$$

Here R_1 and R_2 contain details of the radial components of the LCAO atomic functions and other constant terms. As seen from table 1, there is a considerable difference of polarizations between the states.

It is to be noted that although the LCAO coefficients need to be evaluated when discussing a specific system, the relative polarizations may be derived when there is a weak trigonal distortion and then mixing of the 3d and 4p states is dominated by the tetrahedral component of the potential. In this situation the LCAO coefficients would take the limiting value

$$a_t = a_p = 0 \qquad c_e = 0 \qquad b_p = c_p \qquad b_s = 0 \tag{5}$$

and (4) then simplify to

$$S = P = A = 2(a_e c_p R_1)^2 \qquad Q = A/2. \tag{6}$$

We can approximately characterize the polarizations still further by using the vectors α

Table 2. Relative transition probabilities from the t_2 derived spin–orbit state of C_{3v} to the two e derived spin–orbit states of C_{3v}. The trigonal interaction is the same magnitude as spin–orbit interaction ($\delta = \lambda$).

	E_z	E_x	E_y
ψ_1:	$\frac{2}{3}A$	$\frac{2}{3}A$	$\frac{2}{3}A$
ψ_2:	0	A	A

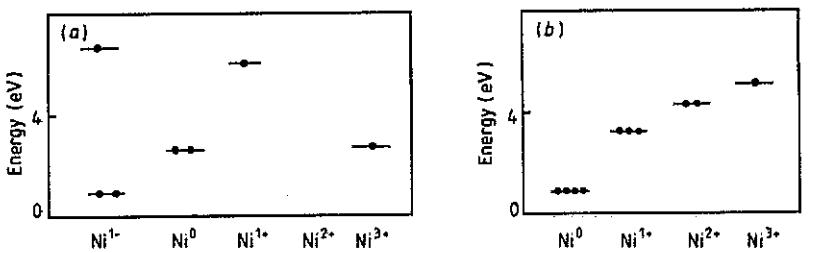

Figure 1. Energies of highest occupied gap states as calculated relative to the top of the valence band for (*a*) substitutional nickel and (*b*) interstitial nickel. The dots indicate the electron occupancy of the energy levels in the gap.

and β which are obtained from (A3) of the Appendix. As a specific example we consider the case where $\delta = \lambda$ which then results in the polarizations shown in table 2.

3. LCAO cluster calculation

To estimate explicitly values of the LCAO coefficients appearing in (3) and (4) we have employed a finite cluster model approach using the CNDO semi-empirical parametrization that has proved suitable to account for several diamond and silicon characteristics (see, for example, Harker and Larkins 1979, Mainwood 1978, Mainwood and Stoneham 1982, Deak *et al* 1987, Lowther 1984). The semi-empirical parameters for transition metals have been obtained from the Clack *et al* (1972) scheme and have been slightly modified (Paslovsky and Lowther 1991) so as to fit known structural properties of nickel oxide molecules (Huber and Herzberg 1979). CNDO parameters employed for carbon were those appropriate to diamond (Harker and Larkins 1979), such a choice being known to predict accurately known structural properties as well as essential details of the energy band structure.

The nickel ion was placed at both substitutional and interstitial tetrahedral locations in clusters $NiC_{16}C^*_{24}$ and $NiC_{18}C^*_{28}$, where C* and sp^3 hybrids that act to saturate the cluster surfaces in the usual way (see Mainwood 1978). In figure 1 we indicate occupied gap states resulting from the calculations, with various cluster charge states being considered for both substitutional and interstitial configurations. Emerging gap states are recognized by comparison with electronic spectra calculated from pure diamond clusters, and Fermi levels obtained from a direct count of the number of electrons in the cluster. The gap states are labelled according to the irreducible representations of the tetrahedral point group T_d and are indicated in the figures as measured from the top of the cluster valence bands, these bands being defined by states that appear virtually unchanged with the inclusion of the nickel impurity—those of symmetry a_1, a_2 or t_1.

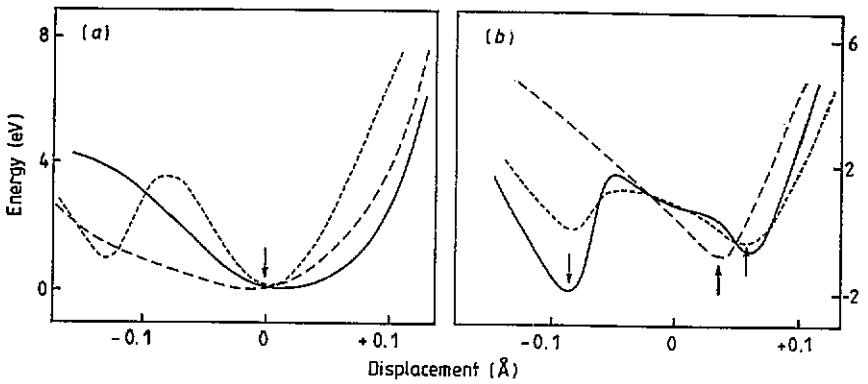

Figure 2. Change in total energy as a function of the nickel ⟨111⟩ displacement for (*a*) substitutional nickel and (*b*) interstitial nickel. (———) Ni^{1-}, (– – –) Ni^{1+}, (— —) Ni^{0}. The +ve displacement is towards the nearest carbon atom, and arrows indicate locations of the energy minima.

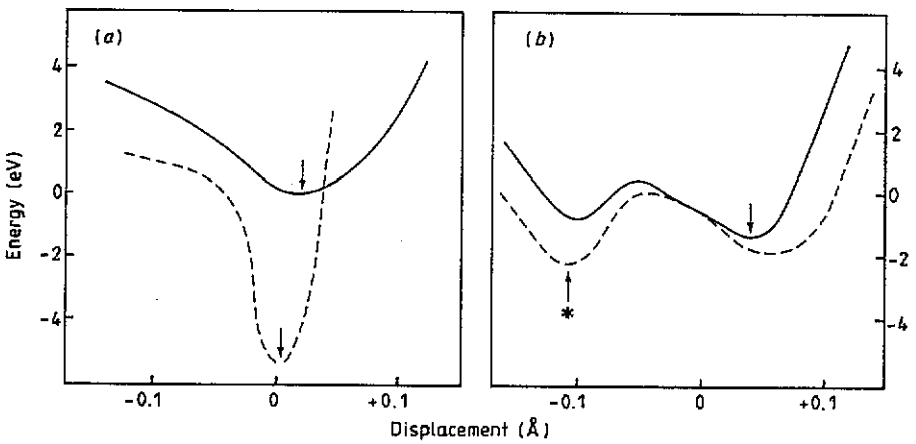

Figure 3. Change in total energy as a function of nickel ⟨111⟩ displacement for (*a*) substitutional Ni^{1-}; and (*b*) interstitial Ni^{1+}. (——) without trigonal relaxation of the carbon atoms, (– – –) with trigonal relaxation. The +ve displacement is towards nearest carbon atom.

Guided by the piezospectroscopic results (Nazare *et al* 1991) that indicate a centre with C_{3v} symmetry for the 1.4 eV lines, we have displaced the nickel defect along a ⟨111⟩ direction in the cluster. In figure 2 we show the behaviour of the cluster total energy with this ⟨111⟩ displacement for several cluster charges and with the nickel located on both the substitutional and interstitial sites. The depth of the potential wells could be taken as some measure of displacement of the ion from the associated sites, however, this point, and especially within the present calculation, should be viewed with some caution. This is because the lattice relaxations are quite large and the potentials appear rather complex with associated secondary relaxations very likely. In fact we have considered such secondary relaxations in which the four surrounding carbon atoms about the defect were allowed to relax both symmetrically outward and also trigonally at each displacement of the nickel defect.

In figure 3 we show the effect of including secondary relaxation on total energies, such total energy curves being typical of the behaviour of other nickel charge states. As

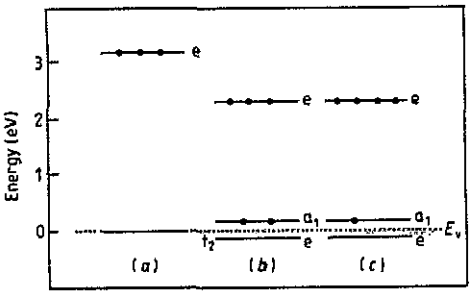

Figure 4. Gap states as measured from top of valence band for interstitial Ni^{1+} in (*a*) T_d symmetry; (*b*) C_{3v} symmetry: the ^2E state; (*c*) C_{3v} symmetry: the $^2A_1$ state. The splitting of the t_2 state is estimated to be ~100 meV. Levels for the energy minima are indicated by * in figure 3(*b*).

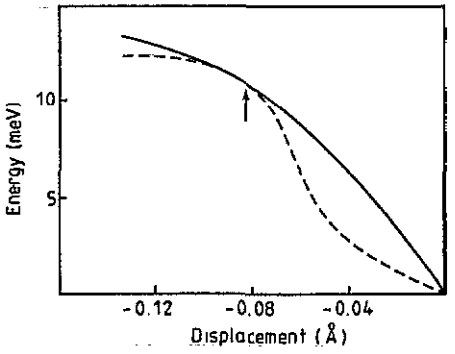

Figure 5. Spin–orbit splitting of the ^2E state as a function of the ⟨111⟩ displacement. (——) without trigonal relaxation, (– – –) with trigonal relaxation. Arrow indicates location of minima in the total energy calculations.

our main point is to investigate the symmetry of the defect with respect to ⟨111⟩ movement, we see that our calculations indicate that the nickel be situated in T_d symmetry on a substitutional site and in C_{3v} symmetry on an interstitial site. The former assignment is consistent with the centre observed by Isoya *et al* (1990) and the latter with the 1.4 eV centre reported by Nazare *et al* (1991).

We now consider specifically the interstitial site, and in figure 4 display gap states developing from Ni^{1+}. First, in figure 4(*a*) we show states for the perfect tetrahedral position and then in figure 4(*b*) how these states are split when there is a ⟨111⟩ movement of the ion and the symmetry descends to C_{3v}. We note that the many-electron state displayed by the one-electron configurations is ^2E. Upon excitation of one of the electrons from the lower a state to the upper e state as depicted in figure 4(*c*), a $^2A_1$ many-electron state arises. The calculated value of the excitation energy is 2.33 eV which is in fair agreement with the observed value of 1.4 eV considering the qualitative nature of the calculation method used. It is also noted that the states involved in the transition that are derived using this method are of orbital A and E character which is consistent with that recently deduced using piezospectroscopy on the 1.4 eV zero phonon lines (Nazare *et al* 1991).

Using (3) we estimate the magnitude of the spin–orbit splitting, and this is shown in figure 5 for varying values of the ⟨111⟩ distortion of the nickel centre. The value for the interstitial site is considerably higher than the observed splitting of 2.7 meV. The high calculated values must be considered with some caution since we must take into account the approximate nature of the model and, more importantly, that we have neglected any Jahn–Teller quenching interactions. In fact, a measure of the quenching factor has been calculated by Lowther and Stoneham (1978) and was found to be ~0.153. Including this factor, our calculated values now fall well within the range of the observed value.

To obtain the optical polarizations we considered several relative cases of spin–orbit and trigonal interaction as measured by the ratio (δ/λ) and here show results for $(\delta/\lambda) = 1$ and $(\delta/\lambda) = 2$. The LCAO coefficients are again taken from our cluster calculation corresponding to the different amounts of displacement of the nickel ion along the ⟨111⟩ direction. The magnitude of the calculated relative transition probabilities of the two energy components are illustrated in figure 6. We see that the relative intensities depend strongly upon the ratio (δ/λ) with the absolute value upon the extent of trigonal

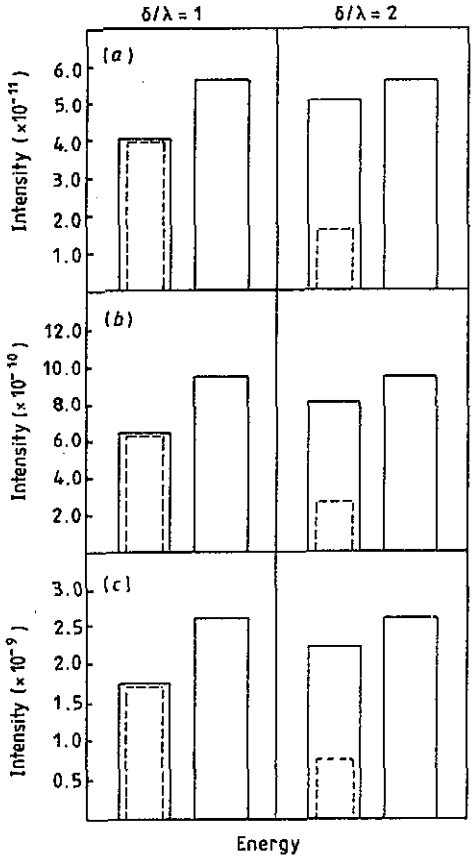

Figure 6. Intensities of the transitions ψ_1 and ψ_2 corresponding to ⟨111⟩ displacements of (*a*) 0.05 Å; (*b*) 0.10 Å; and (*c*) 0.15 Å. $\delta/\lambda = 1$ and $\delta/\lambda = 2$ is considered in each case. (– – –) E_z polarization and (——) E_x or E_y polarizations.

distortion. This feature corresponds to the degree of localization of the metal wavefunctions at the ion site and therefore the depth of the defect level in the energy gap of the diamond host. All intensites depend strongly upon the ⟨111⟩ atom displacement with an increase in intensity corresponding to larger trigonal relaxation. This relates to the strong build up of 4p character in the lower one-electron t_2 derived states as the metal defect levels become more localized.

4. Discussion

Our calculations support the suggestion that the 1.4 eV doublet in diamond arises from optical transitions at a nickel defect and at which there is a substantial degree of electronic hybridization as well as lattice deformation. We have shown that the relative intensities of the two doublet components are readily accounted for in a theory which attributes the doublet to a spin–orbit mechanism. The polarization in one of the 1.4 eV components, which is observed to differ by less than 30% in π or σ orientation, is also consistent with a model in which the spin–orbit perturbation of the electron states very nearly equals the trigonal perturbation. Although it had not been necessary to make recourse to numerical computation to arrive at these conclusions we found that a LCAO cluster model calculation gave a further understanding of states of the nickel defect, and again quantitatively supported the spin–orbit model for the origin of the 1.4 eV doublet.

The cluster model calculation strongly suggested that the doublet arises from an Ni^{1+} interstitial defect at which there is a significant degree of lattice relaxation.

Recent experimental evidence could support our suggestion that the 1.4 eV lines are due to Ni^{1+}. Collins *et al* (1990) showed that the intensity of the 1.4 eV lines decreases when increasing amounts of nitrogen are present in the diamond. As nitrogen is usually a donor in diamond,the implication of such an observation is that the donor electron is being transferred to the Ni^{1+} centre and, in doing so, lowering the concentration of optially active Ni^{1+} ions.

Acknowledgments

We are grateful to the FRD for their support especially L Paslovsky for the award of a FRD research studentship. We would also like to thank Dr Gordon Davies for keeping us informed of recent spectroscopic results on diamond.

Appendix

In analysing the inclusion of the spin–orbit interaction it proves convenient to represent the t_2 (d_ε, d_η, d_ξ) d-electron states as follows

$$\begin{aligned} d_{+1} &\equiv |+1\rangle = -i(d_\xi + id_\eta)/\sqrt{2} \\ d_0 &\equiv |0\rangle = id_\zeta \\ d_{-1} &\equiv |-1\rangle = i(d_\xi - id_\eta)/\sqrt{2}. \end{aligned} \tag{A1}$$

Table A1. Spin orbit wave-functions: tetrahedral point symmetry.

Γ_7:	$-\sqrt{\frac{1}{3}}\|0\rangle^{\pm} + \sqrt{\frac{2}{3}}\|\pm 1\rangle^{\mp}$
Γ_8:	$\theta^{\pm}$; $\varepsilon^{\pm}$
	$\|\mp 1\rangle^{\mp}$
	$\sqrt{\frac{2}{3}}\|0\rangle^{\pm} + \sqrt{\frac{1}{3}}\|\pm 1\rangle^{\mp}$

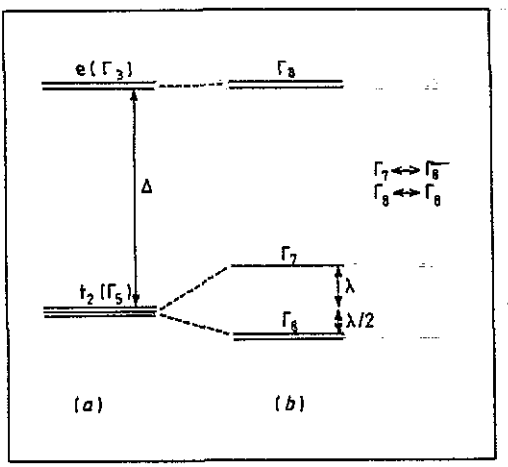

Figure A1. Energy level scheme of d states for tetrahedral environment T_d (*a*) without spin–orbit coupling; and (*b*) with spin–orbit coupling. Selection rules included.

Recalling that in the tetrahedral environment the spin–orbit interaction does not split the e state and neglecting any second order terms ($\Delta \gg \lambda$), the spin–orbit matrix associated with the t_2 electrons is given by

$$\begin{array}{c} \quad |+1\rangle^- \quad |-1\rangle^- \quad |0\rangle^+ \\ \begin{bmatrix} \lambda/2 & 0 & -\lambda/\sqrt{2} \\ 0 & -\lambda/2 & 0 \\ -\lambda/\sqrt{2} & 0 & 0 \end{bmatrix} \end{array} \tag{A2}$$

The matrix describing the other Kramers set of states may be similarly derived. A simple unitary transformation diagonalizes (A2) leading to the states listed in table A1. The allowed optical transitions between those states are indicated in figure A1.

Lowering in point symmetry of the tetrahedral environment from that of T_d to C_{3v} produces a splitting of the $t_2(\Gamma_5)$ degenerate state into trigonal states $a_1(\Gamma_1)$ and e (Γ_3), as illustrated in figure A2. In the presence of spin–orbit coupling, the orbital trigonal e state is further split into a series of Kramers doublets. If second-order effects are

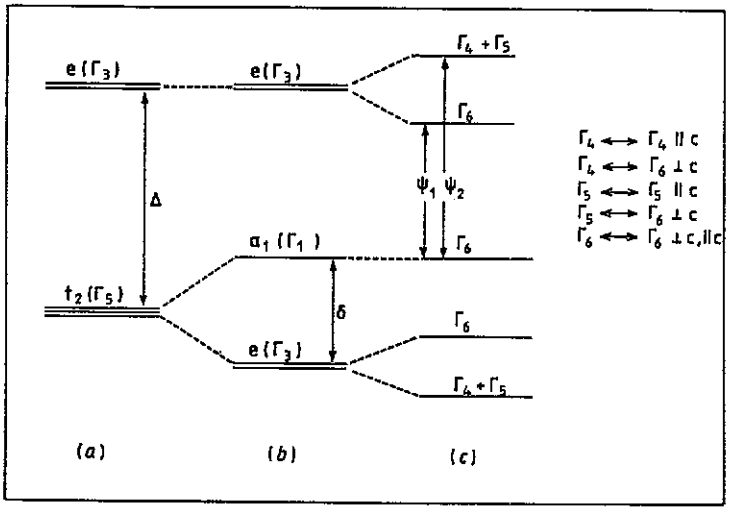

Figure A2. Energy level scheme of d states for (*a*) tetrahedral environment T_d; (*b*) for trigonal environment C_{3v} without spin–orbit coupling; and (*c*) with spin–orbit coupling. Selection rules for trigonal environment C_{3v} are included.

Table A2. Spin–orbit wave-functions: trigonal point symmetry. The x, y, and z functions would be directed along $\langle 1\bar{1}0\rangle$, $\langle 11\bar{2}\rangle$ and $\langle 111\rangle$ axes of the tetrahedron. Vectors (α, β) are obtained numerically from (A3).

$\Gamma_4 + \Gamma_5$: Γ_6:	$\begin{matrix} \sqrt{\frac{1}{2}}(x^{\mp} \mp iy^{\mp}) \\ \sqrt{\frac{1}{2}}(x^{\mp} \pm iy^{\mp}) \end{matrix}$	$C_{3v}(e)$
Γ_6:	$\mp\alpha z^{\pm} + \beta\sqrt{\frac{1}{2}}(x^{\mp} \pm iy^{\mp})$	$C_{3v}(a_1)$

neglected ($\delta \ll \Delta$) the resulting spin–orbit states derived from the orbital trigonal states are obtained as follows

$$\begin{array}{c} \quad z^- \quad x^+ \quad y^+ \\ \begin{bmatrix} 2\delta & \lambda & i\lambda \\ \lambda & 0 & -i\lambda \\ -i\lambda & i\lambda & 0 \end{bmatrix} \end{array} \tag{A3}$$

where the x, y and z functions would be directed along the $\langle 1\,-1\,0\rangle$, $\langle 1\,1\,-2\rangle$, and $\langle 1\,1\,1\rangle$ axes respectively of the tetrahedron.

Wave-functions corresponding to the states illustrated in figure A2 are listed in table A2. Values of α and β are obtained numerically from (A3) and essentially are dependent on the ratio δ/λ. Optical (electric dipole) selection rules derived through group theoretic arguments are indicated in figure A2, and are in agreement with the results derived by Birman (1960).

References

Bates C A 1968 *J. Phys. C: Solid State Phys.* **1** 870–9
Birman J 1960 *J. Electrochem. Soc.* **107** 409–17
Clack D W, Hush N S and Yandle J R 1972 *J. Chem. Phys.* **57** 3503–10
Collin A T 1989 *J. Phys.: Condens. Matter* **1** 439–49
Collins A T, Kanda H and Burns R C 1990 *Phil. Mag.* **61** 797–810
Collins A T and Spear P M 1983 *J. Phys. C: Solid State Phys.* **16** 963–78
Davies G, Neves A J and Nazare M E 1989 *Europhys. Lett.* **9** 47–52
Deak P, Snyder L C, Singh R K, Corbett J W 1987 *Phys. Rev.* B **36** 9612–27
Dunn T M 1961 *Trans. Faraday Soc.* **57** 1441–7
Griffith J S 1964 *The Theory of Transition-metal Ions* (London: Cambridge University Press)
Haldane F and Anderson P W 1976 *Phys. Rev.* B **13** 2553–7
Harker A H and Larkins F P 1979 *J. Phys. C: Solid State Phys.* **12** 2487–508
Huber K P and Herzberg G 1979 *Molecular Spectra and Molecular Structure* vol 4 (New York: Van Nostrand)
Isoya J, Kanda H, Norris J R, Tang J and Bowman M K 1990 *Phys. Rev.* B **41** 3905–13
Lowther J E 1984 *Phys. Lett.* **104A** 273–6
Lowther J E and Stoneham A M 1978 *J. Phys. C: Solid State Phys.* **11** 2165–9
Ludwig G W and Woodbury H H 1962 *Solid State Physics* vol 13 (New York: Academic) pp 223–304
Mainwood A 1978 *J. Phys. C: Solid State Phys.* **11** 2703–10
Mainwood A, Stoneham A M 1982 *Physica* **116B** 101–5
Nazare M, Neves A and Davies G 1991 *Phys. Rev.* B **43** 14196–201
Paslovsky L and Lowther J E 1991 *Solid State Commun.* at press
Zunger A 1986 *Solid State Physics* vol 39 (New York: Academic) pp 275–464